AIP Journal of Applied Physics

Stochastic behavior of nanoscale dielectric wall buckling

Lawrence H. Friedman, Igor Levin, and Robert F. Cook

Citation: Journal of Applied Physics **119**, 114305 (2016); doi: 10.1063/1.4943615
View online: http://dx.doi.org/10.1063/1.4943615
View Table of Contents: http://scitation.aip.org/content/aip/journal/jap/119/11?ver=pdfcov
Published by the AIP Publishing

Articles you may be interested in
On the stochastic behaviors of locally confined particle systems
Chaos **25**, 073121 (2015); 10.1063/1.4927300

A high-performance dielectric elastomer consisting of bio-based polyester elastomer and titanium dioxide powder
J. Appl. Phys. **114**, 154104 (2013); 10.1063/1.4824805

Set-based corral control in stochastic dynamical systems: Making almost invariant sets more invariant
Chaos **21**, 013116 (2011); 10.1063/1.3539836

Buckling of defective carbon nanotubes
J. Appl. Phys. **106**, 113503 (2009); 10.1063/1.3261760

Fluctuation-induced interactions between dielectrics in general geometries
J. Chem. Phys. **129**, 014703 (2008); 10.1063/1.2949508

The new SR865 2 MHz Lock-In Amplifier ... $7950

Chart recording
FFT displays
Trend analysis

Features
· Intuitive front-panel operation
· Touchscreen data display
· Save data & screen shots to USB flash drive
· Embedded web server and iOS app
· Synch multiple SR865s via 10 MHz timebase I/O
· View results on a TV or monitor (HDMI output)

Specs
· 1 mHz to 2 MHz
· 2.5 nV/√Hz input noise
· 1 µs to 30 ks time constants
· 1.25 MHz data streaming rate
· Sine out with DC offset
· GPIB, RS-232, Ethernet & USB

SRS Stanford Research Systems
www.thinkSRS.com · Tel: (408)744-9040

Reuse of AIP Publishing content is subject to the terms at: https://publishing.aip.org/authors/rights-and-permissions. Download to IP: 129.6.180.62 On: Thu, 17 Mar 2016 12:30:09

JOURNAL OF APPLIED PHYSICS 119, 114305 (2016)

Stochastic behavior of nanoscale dielectric wall buckling

Lawrence H. Friedman, Igor Levin, and Robert F. Cook[a]
Materials Measurement Science Division, National Institute of Standards and Technology, 100 Bureau Drive, Gaithersburg, Maryland 20899, USA

(Received 16 December 2015; accepted 27 February 2016; published online 16 March 2016)

The random buckling patterns of nanoscale dielectric walls are analyzed using a nonlinear multi-scale stochastic method that combines experimental measurements with simulations. The dielectric walls, approximately 200 nm tall and 20 nm wide, consist of compliant, low dielectric constant (low-*k*) fins capped with stiff, compressively stressed TiN lines that provide the driving force for buckling. The deflections of the buckled lines exhibit sinusoidal pseudoperiodicity with amplitude fluctuation and phase decorrelation arising from stochastic variations in wall geometry, properties, and stress state at length scales shorter than the characteristic deflection wavelength of about 1000 nm. The buckling patterns are analyzed and modeled at two length scales: a longer scale (up to 5000 nm) that treats randomness as a longer-scale measurable quantity, and a shorter-scale (down to 20 nm) that treats buckling as a deterministic phenomenon. Statistical simulation is used to join the two length scales. Through this approach, the buckling model is validated and material properties and stress states are inferred. In particular, the stress state of TiN lines in three different systems is determined, along with the elastic moduli of low-*k* fins and the amplitudes of the small-scale random fluctuations in wall properties—all in the as-processed state. The important case of stochastic effects giving rise to buckling in a deterministically sub-critical buckling state is demonstrated. The nonlinear multiscale stochastic analysis provides guidance for design of low-*k* structures with acceptable buckling behavior and serves as a template for how randomness that is common to nanoscale phenomena might be measured and analyzed in other contexts.
[http://dx.doi.org/10.1063/1.4943615]

I. INTRODUCTION

The central limit theorem of statistics[1,2] tells us that the effect of random fluctuations on the mean properties of an object should increase as the size of the object decreases—approximately as the inverse square-root of object volume. Hence, nanoscale components and materials incorporating nanoscale structure are subject to enhanced variability and randomness, leading to challenges in quantitative nanoscale materials science and engineering. Other challenges related to nanoscale components and materials have received much attention, such as the need for precise dimensional metrology,[3] the computational property determination,[4,5] and the presence of size effects.[6–9] It has also been observed that hierarchical models of materials behavior must incorporate the effects of the stochastic nature of materials, particularly at smaller scales.[10] It is less commonly noted, however, that the behavior of smaller components and microstructures is more sensitive to uncontrollable fluctuations in geometry and properties. Generalized stochastic models incorporating such fluctuations can be cumbersome to develop and analyze, however, and it is thus helpful to find simple problems that are technologically or scientifically worthy of study such that specific stochastic models can be developed and applied. The random buckling of nanoscale interlayer dielectric (ILD) trench walls (Fig. 1 and Refs. 11–16) is such a problem.

Buckling occurs in slender structures under large compressive loads: The compressive load overwhelms the stiffness of the structure so that it deflects (buckles) perpendicularly to the direction of load. The most well-known example is Euler-buckling of columns,[17] in which the maximum compressive load that can be supported by a column before buckling is proportional to the column second areal moment but inversely proportional to the square of the column length. Hence, slender (large length/transverse dimension) structures are susceptible to buckling. The problem of nanoscale dielectric wall buckling arises in microelectronics devices, in which performance can be enhanced by using nano-width metal electrical interconnection lines lying in low-permittivity (low-*k*) ILD trenches with nano-width walls.[13] Unfortunately, the technological electrical requirements for nanoscale ILD trenches coincide with the criteria for mechanical buckling of the trench walls. ILD trenches are often lithographically patterned using a hard TiN mask with large Young's modulus (150 GPa to 400 GPa) and incorporating a large compressive stress (>1 GPa). The thin mask is etched into long, thin strips and without additional support these slender structures would surely buckle. The underlying ILD trench wall stabilizes the TiN strips against buckling, but only weakly. The low electrical permittivity of the ILD is accompanied by small Young's modulus (∼10 GPa), and ILD walls must be slender for enhanced interconnect density and tall for reduced electrical resistance of the intervening metal, all characteristics that reduce their ability to mechanically stabilize the TiN hard mask. Consequently, the trench walls frequently buckle *en masse*, forming oscillatory patterns characterized by large randomness evident in amplitude fluctuations and poor phase correlation

[a]Author to whom correspondence should be addressed. Electronic mail: robert.cook@nist.gov.

Reuse of AIP Publishing content is subject to the terms at: https://publishing.aip.org/authors/rights-and-permissions. Download to IP: 129.6.180.62 On: Thu, 17 Mar 2016 12:30:09

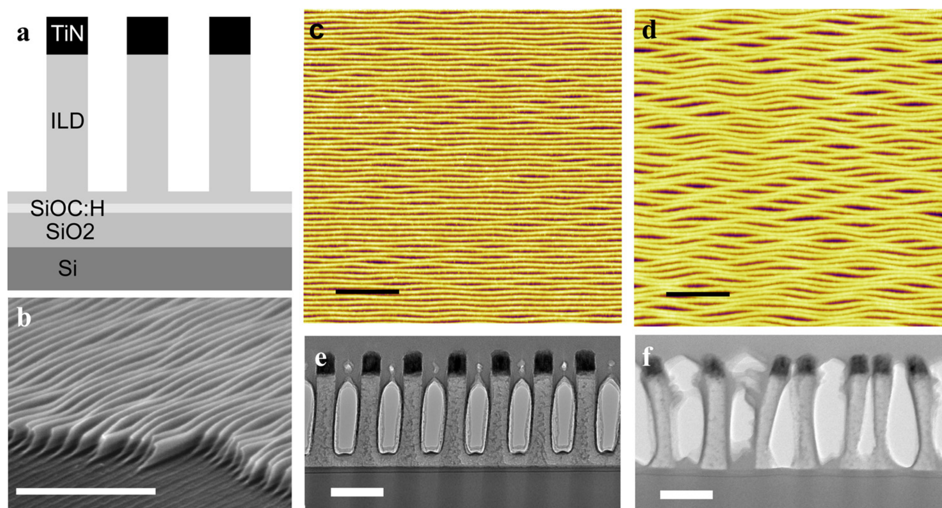

FIG. 1. Buckled ILD trench walls capped with TiN hardmask. (a) Schematic cross section of complete stack of TiN-masked ILD trenches on a Si wafer. (b) Scanning electron microscope (SEM) image of masked ILD trench walls (from Sample S1). In the foreground, the ILD walls have been scratched off to reveal wall height and deflected wall profile. Scale-bar is 1 μm. (c) and (d) AFM images of buckled trench walls from samples S2 and S3, respectively. Scale-bars are 1 μm. (e) and (f) Cross-section TEM images of samples S2 and S3, respectively. Scale-bars are 100 nm.

(Figs. 1(b)–1(d)). Due to the technological implications of high performance interconnects,[11,12] it is desirable to have a validated quantitative model that allows buckled arrays of ILD walls to be analyzed and to assist in structure and process design to avoid buckling in future iterations. This need can only be fully met with a model that is both nonlinear and stochastic.

Prior quantitative treatment of ILD trench wall buckling has applied linear deterministic methods.[13,15,16] Deterministic buckling models inevitably predict the formation of perfectly periodic deflections; however, measured buckling deflections are clearly pseudo-periodic, exhibiting both phase decorrelation and amplitude fluctuations (Figs. 1(b)–1(d)). More broadly, nanoscale and microscale buckling have some history in the literature including nonlinear modeling, but with less attention paid to random behavior. Some studied systems had negligible randomness,[18–24] where the need for extensive analysis could be intuitively dismissed. These instances tended to occur at the micro-scale. In other studies, randomness was simply neglected based on the assumption that deterministic models could provide sufficiently accurate predictions of mean observations.[25–31] A problem with this assumption for both ILD trench wall models and other buckling models was that it rendered qualitative validation of models through comparison with experiment suspect; a deterministic model will always appear too ideal, so belief that stochastic effects are negligible must be maintained when making the comparison. Equally important, it remained untested whether the fundamental differences between stochastic experimental systems and deterministic models might give rise to quantitative errors in predictions and inferred values. Recently, it was hypothesized that large deviations from deterministic models of trench-wall buckling might result from stochastic effects.[16] The importance of incorporating randomness in models used for prediction or analysis will vary from system to system and with the quantitative inferences to be drawn, but the importance will not be known *a priori*.

In other contexts, randomness has been treated directly. For example, in modeling or analyzing systems with large thermal fluctuations, randomness was understood *a priori*, e.g., Refs. 32–34. In some examples of multiscale modeling and measurement, shorter-scale randomness was measured and modeled but then homogenized to create a longer-scale deterministic model, e.g., Refs. 35–40. In the case of interest, ILD trench wall buckling, longer-scale observed random behavior (the aforementioned buckling amplitude variability and phase decorrelation) results from random fluctuations at smaller scales that cannot possibly be measured directly: In particular, local variations in the TiN compressive stress, in the cross-sectional geometry of the ILD trench wall and overlying TiN mask, and in the elastic moduli of the ILD and mask all lead to small-scale random fluctuations in the driving and resisting forces, and hence net force, for wall buckling.

To overcome this challenge, the shorter-scale randomness is determined here indirectly from its measurable effects at the longer scale. Although somewhat counterintuitive, this approach serves to determine both the qualitative and quantitative effects of randomness. The approach is akin to a rider in a car determining how smooth or bumpy a road is from knowledge of how their car works and how the ride feels; direct inspection of the bumps is not required. Three samples of buckled ILD trench wall structures are analyzed here using measurements and modeling at two length scales. The shorter-scale ranges from about 20 nm, the smallest cross-sectional dimension, to about 500 nm, the half-wavelength of a typical buckling oscillation. This scale is the domain of buckling mechanics. The longer-scale ranges from about 500 nm to 5000 nm and is important for modeling and interpreting the gross buckling morphology. The resulting simulations of randomness in trench-wall deflections are compared with experimental measurements. Inferred material properties and state of ILD trench walls and hard-mask are compared with measurements of similar materials and measurements made prior to lithography, and stochastic effects on inferred properties and state are assessed. All analysis inputs come from measurements of as-processed samples, an important consideration when the possible effects of etching on material state and property are considered.[15]

II. MATERIALS AND MICROSCOPY

Transmission electron microscopy (TEM) and atomic force microscopy (AFM) measurements of samples of three patterned ILD structures (S1, S2, and S3) were studied. The ILD samples were used in a similar study[16] and correspond to

Reuse of AIP Publishing content is subject to the terms at: https://publishing.aip.org/authors/rights-and-permissions. Download to IP: 129.6.180.62 On: Thu, 17 Mar 2016 12:30:09

TABLE I. Measured properties and deflection statistics of buckled walls.

	Sample S1	Sample S2	Sample S3
TiN Young's modulus, E_{TiN} (GPa)[a]	210 ± 17	186 ± 14	186 ± 14
Wall height (nm)[b]	200 ± 2	206 ± 1	223 ± 2
Mean square-deflection, $\overline{\nu^2}$ (nm^2)[c]	206 ± 14	47.0 ± 3.9	462 ± 34
Fourth moment of deflection, $\overline{\nu^4}$ (10^3 nm^4)[c]	78.4 ± 9.4	5.74 ± 0.99	417 ± 55

[a]As reported.[16]
[b]± value indicates standard deviation of measurements.
[c]± value indicates standard error of fitted mean.

samples C, A, and B therein. Each sample had different dimensions or materials and different buckling characteristics.

A. Patterned ILD structures

The stack structure of the patterned ILD samples (Fig. 1(a)) consisted of five layers.[16] From bottom to top: Layer 1 was a 300 mm diameter (100) Si wafer. Layer 2, 100 nm SiO_2, was deposited by chemical vapor deposition (CVD) directly on the Si wafer. Layer 3, 2 nm dense ($k = 4.8$) SiOC:H etch stop film, was deposited by plasma enhanced CVD (PECVD).[41] Layer 4, low-k a-SiOC:H ($k = 2.65$, sample S1) or a-C:H ($k = 2.25$, samples S2 and S3) ILD films, was deposited on the SiO_2/SiOC:H film stack by PECVD[42] and spin-on deposition, respectively.[43] Layer 5, 20 nm to 40 nm TiN hardmask, was deposited by standard physical vapor deposition methods.[13]

The ILD geometry consisted of long patterned trenches with thin, high aspect-ratio walls as in Fig. 1, as well as wide regions (~300 nm) of unetched area that enabled measurement of the TiN modulus of each sample, Table I.[16] The trench walls areas exhibited buckling and were the focus of study. Etching depth (wall-height) is one of the main parameters that determines buckling:[13,15,16] Sample S2 (Figs. 1(c) and 1(e)) has a width similar to sample S3 (Figs. 1(d) and 1(f)), about 35 nm, but a different height. Sample S2 is 206 nm tall, while sample S3 is 223 nm tall. The larger buckling amplitude of the more deeply etched sample S3 is clear.

B. Cross-sectional microscopy

Precise measurements of the ILD trench wall cross-sections were obtained from TEM. Samples were prepared using a focused ion beam. Both high-resolution TEM and high-angle dark field scanning TEM (STEM) images were recorded using an FEI Titan TEM/STEM (Hillsboro, Oregon)[44] operated at 300 kV. Overall heights and width profiles as well as the boundaries between the TiN mask and the ILD were measured from TEM images. Slight variations in the widths were observed along the walls. See Appendix A[45] for more details. Average wall heights for each sample are reported in Table I. These measured dimensions were used as inputs for finite element modeling (FEM).

C. Buckling deflections

AFM measurements of buckled ILD trench walls were provided (Figs. 1(c) and 1(d)) for each sample along with inferred buckling deflections, v, vs. position, x, $v(x)$. Fig. 2(a) shows examples of measured lateral deflections of ILD trench walls (black lines). (It will be shown later that the deflection uncertainty was about ±0.8 nm as indicated by modeling of the high-frequency statistical noise (Appendix C.3 (Ref. 45)).) The pseudo-periodic nature of the deflections is clearly seen when contrasted with idealized periodic oscillations of similar lateral scales and magnitudes (thick pink lines).

The pseudo-periodic deflections can best be described as a stationary random (or stochastic) process.[46,47] Thus, a robust characterization of the ILD trench-wall buckling must employ stochastic methods. As each measured deflection profile contained only a small number of oscillations, it seemed that real-space methods for deflection analysis would provide better precision and detail than reciprocal-space methods. The deflection autocorrelation was calculated for each sample: $C_v(\Delta x) \stackrel{\text{def}}{=} \overline{v(x)v(x+\Delta x)}$, where the overbar indicates an average over all measured x values and all line

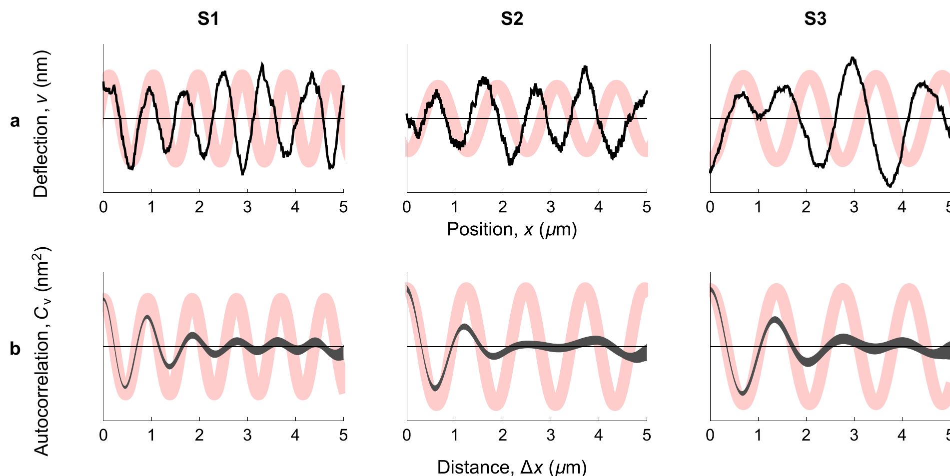

FIG. 2. Measured long-scale buckling morphology for samples S1, S2, and S3. (a) Black lines show examples of deflection profiles measured by AFM. Pink periodic sinusoids with constant amplitude and perfect phase correlation are shown in the background for contrast. Both black and pink curves have the same characteristic wavenumber and root mean-square amplitude. (b) Deflection autocorrelations: Dark-gray shows uncertainty band for mean measured autocorrelation at approximately 95% confidence (two standard deviations). Pink periodic sinusoids are shown in the background illustrating autocorrelation for hypothetical deterministic case with constant amplitude and perfect phase correlation.

Reuse of AIP Publishing content is subject to the terms at: https://publishing.aip.org/authors/rights-and-permissions. Download to IP: 129.6.180.62 On: Thu, 17 Mar 2016 12:30:09

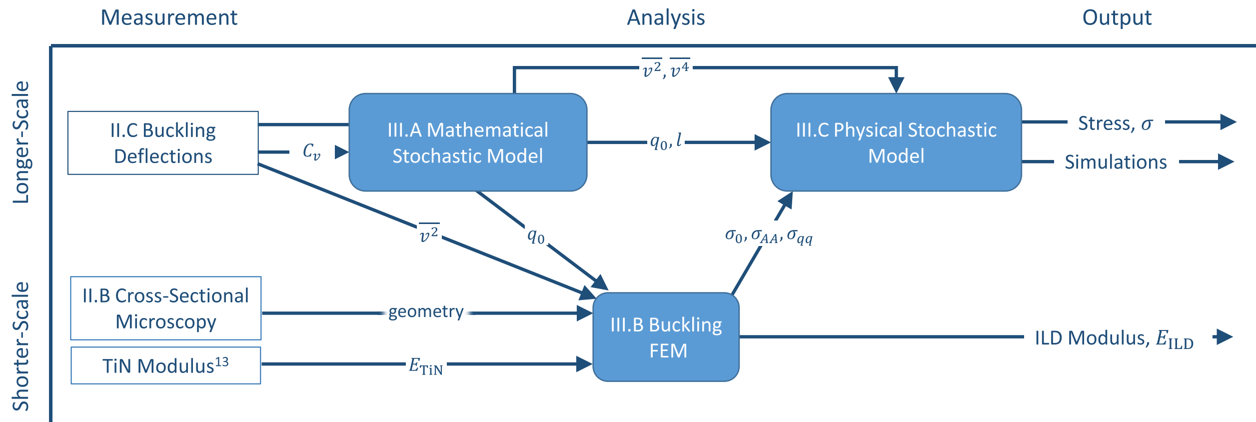

FIG. 3. Diagram of the information flow for the nonlinear multiscale stochastic buckling analysis. The measurements and analyses are labeled by section number in text.

profiles. It also proved very important to characterize the amplitude fluctuations, so the fourth deflection moment ($\overline{v^4}$) was also calculated. Fig. 2(b) shows the autocorrelations for samples S1, S2, and S3 as dark-gray bands, each calculated from about 160 ILD trench wall deflections. The width of the bands indicates the estimated uncertainty at about 95% confidence. The value at zero separation is the mean-square deflection, $\overline{v^2} = C_v(0)$. See Appendix B[45] for numerical details. Oscillations in the autocorrelation indicate the characteristic wavenumber, while the decay of the autocorrelation to zero for large values of Δx indicates phase decorrelation. The decay is to be contrasted with the infinite-range autocorrelation of a sinusoid with perfect phase coherence (Fig. 2(b), thick pink lines). Three 5-μm square AFM images of different locations were analyzed for each sample.

III. STOCHASTIC MULTILSCALE ANALYSIS

The stochastic multiscale analysis of the buckling data had three stages, beginning with longer-scale analysis, moving to shorter-scale methods, and then returning to the longer scale. The longer-scale analyses employed stochastic methods that extracted information from the manifest random behavior of the ILD-trench wall deflections, while the shorter-scale analysis employed exclusively deterministic methods to avoid the burden (or impossibility) of measuring shorter-scale randomness. The information flows between the length-scales, measurements, analysis stages, and expected results are illustrated in Fig. 3.

In the first stage, longer-scale modeling and measurements were used to generate a succinct statistical description of the pseudo-periodic buckling of the ILD-trench walls. In the second stage, shorter-scale buckling mechanics was modeled via FEM using inputs from the first stage statistical analysis and the TEM cross-section measurements. Measured mechanical properties[16] were used to calibrate the overall stress scales of the FEM outputs. In the third stage, the first-stage mathematical stochastic model was refined using statistical inputs from the first stage of analysis and calibrated physical inputs from the shorter-scale second stage of analysis. The refined physical model was then used to extract the TiN mask stress and to simulate buckling deflections for method validation. Input and output quantities are given in Table II.

A. Mathematical stochastic model

The purpose of the first analysis stage was to extract useful information from the measured deflection autocorrelations

TABLE II. Quantities used in and obtained from nonlinear multiscale stochastic buckling analysis.

	Sample S1	Sample S2	Sample S3
Characteristic wave number, q_0 (rad μm^{-1})[a]	6.803 ± 0.041	5.071 ± 0.042	4.547 ± 0.040
Correlation length, l (nm)[a]	701 ± 36	554 ± 30	805 ± 51
Characteristic wavelength, λ_0 (nm)[b]	923.6 ± 5.6	1239 ± 10	1381 ± 12
ILD modulus ratio, E_{ILD}/E_{TiN} (10^{-3})	23.1	24.4	25.3
ILD modulus, E_{ILD} (GPa)	4.85	4.54	4.71
Critical stress, σ_0 (GPa)	1.715	1.632	1.178
Wavenumber sensitivity, σ_{qq} (GPa μm^2)	92.4	138.5	113.5
Amplitude sensitivity, σ_{AA} (MPa nm^{-2})	2.73	1.277	1.057
Phase decorrelation, r_{pd}	0.0836	1.880	0.0894
Amplitude fluctuation, r_{af}	1.230	1.733	1.302
Stochastic correction, $f(r_{pd}, r_{af})$	0.861	−0.934	0.818
Inferred TiN stress, σ (GPa)	2.68	1.520	1.978
Fractional stochastic stress correction (%)	−5.8	−15.3	−9.0

[a]± value indicates standard error from fit.
[b]± value propagated from q_0 estimated uncertainty.

Reuse of AIP Publishing content is subject to the terms at: https://publishing.aip.org/authors/rights-and-permissions. Download to IP: 129.6.180.62 On: Thu, 17 Mar 2016 12:30:09

(Sec. II C), namely, the characteristic deflection wavenumber, q_0, and the phase decorrelation length, l. Initially, the empirical autocorrelations were fit with exponentials or Gaussians that modulated sinusoidal oscillations. This function-guessing approach failed to give good fits to the data and lacked any connection to an appropriate physical or mathematical model. To find a better and more meaningful fit, a common mathematical model describing stable pattern formation[48] was chosen and augmented with stochastic perturbing forces. This model allowed the autocorrelations to be expressed using only a few parameters that could be incorporated into later analysis stages.

The mathematical stochastic model employs the method of amplitude functions that was developed to describe convection flows[49,50] and has since gained broad use in the study of pattern formation.[48] The buckling deflection $v(x)$ was decomposed into a product of a spatially varying complex amplitude function, $A(x)$, and a regular periodic oscillation such that $v(x) = \mathrm{Re}[A(x)\, e^{iq_0x}]$.[48] The role of $A(x)$ in describing a spatially varying amplitude is illustrated in Fig. 4, in which the modeled deflection (black) oscillates between the upper and lower bounds, $\pm|A(x)|$ (gray). The phase decorrelation results from variations in the complex phase of $A(x)$ (not shown). For the longer-scale governing equation, a variant of the ubiquitous Ginzburg-Landau (G-L) form was used that is useful for describing pattern formation with stable characteristic wavenumber and amplitude[48,51]

$$\left[\sigma_{AA}\left(|A(x)|^2 - A_0^2\right) - \frac{1}{2}\sigma_{qq}\partial_x^2\right]A(x) = F(x), \quad (1)$$

where A_0 is the equilibrium amplitude of an unperturbed system, σ_{AA} and σ_{qq} are unknown coefficients, and $F(x)$ is the perturbing generalized stochastic force. Later, the unknown σ_{AA} and σ_{qq} are shown to be the sensitivities of the buckling stress to deflection amplitude and wavenumber, respectively (Sec. III C). The perturbing force, $F(x)$ (right side), represents the random fluctuations occurring throughout the ILD walls and TiN caps that would tend to drive the departure of buckling from perfect periodicity, for example, geometric imperfections and fluctuations in stiffness and stress. The form of the perturbing force was determined phenomenologically by finding the simplest mathematical expression capable of simulating the observed stochastic fluctuations as discussed in Sec. III C. The G-L form (left side) can be derived more rigorously using the method of multiple scales and assumes that the buckling behavior is only weakly nonlinear. Similar weakly nonlinear approximations have been applied to deterministic film buckling.[21,29,30] Further discussion of the form of Eq. (1) is given in Appendix C.1.[45]

Despite its abstract form and unknown coefficient values, Eq. (1) is very useful: Setting $F(x)$ as additive white noise, Eq. (1) was solved approximately for the autocorrelation of the amplitude function, $C_A(\Delta x)$. Subsequently, the autocorrelation of the deflection was found to have the form

$$C_v(\Delta x) = \overline{v^2}\left(1 + \frac{|\Delta x|}{l}\right)\exp\left(-\frac{|\Delta x|}{l}\right)\cos(q_0|\Delta x|), \quad (2)$$

a sinusoidal oscillation that is damped by a modified exponential envelope function, where $\overline{v^2}$ is the mean-square deflection, l is the correlation length, and q_0 is the characteristic wavenumber. Derivation details are in Appendix C.2.[45] Using the measured values of $\overline{v^2}$ and the autocorrelations (Sec. II C), Eq. (2) was fit using maximum likelihoods to obtain values of q_0 and l for each sample. Figure 5 shows the best fit damping envelopes overlaying the experimental autocorrelations. Simulated autocorrelations (Sec. III C) are also shown.

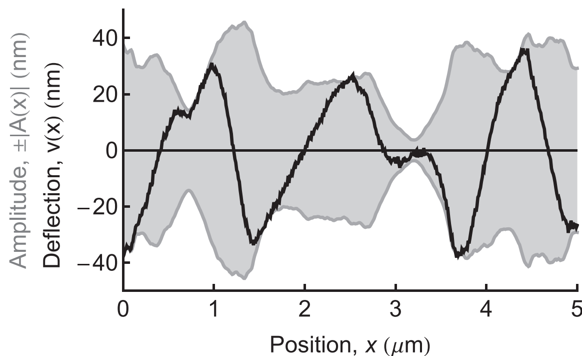

FIG. 4. Simulated deflection using method of amplitude functions corresponding to sample S3. Black line shows deflection, $v(x)$. Gray envelope shows plus and minus the absolute value of the spatially varying amplitude ($\pm|A(x)|$). The phase of $A(x)$ can be inferred from the relation between the black and gray lines.

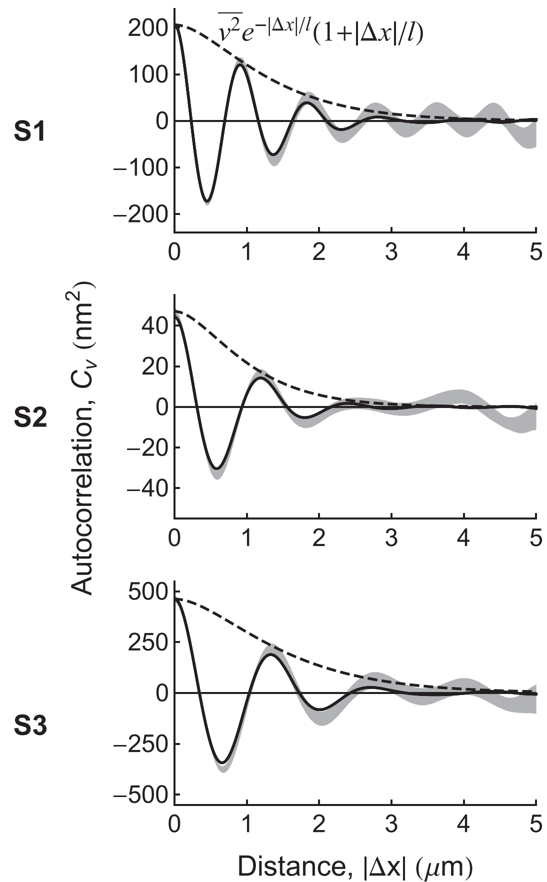

FIG. 5. Deflection autocorrelations for samples S1, S2, and S3. Gray shows uncertainty band for mean measured autocorrelation at approximately 95% confidence (two standard deviations); dashed lines show the best-fit autocorrelation envelope function (Eq. (2)); solid lines show the mean of 4000 simulated autocorrelations.

Reuse of AIP Publishing content is subject to the terms at: https://publishing.aip.org/authors/rights-and-permissions. Download to IP: 129.6.180.62 On: Thu, 17 Mar 2016 12:30:09

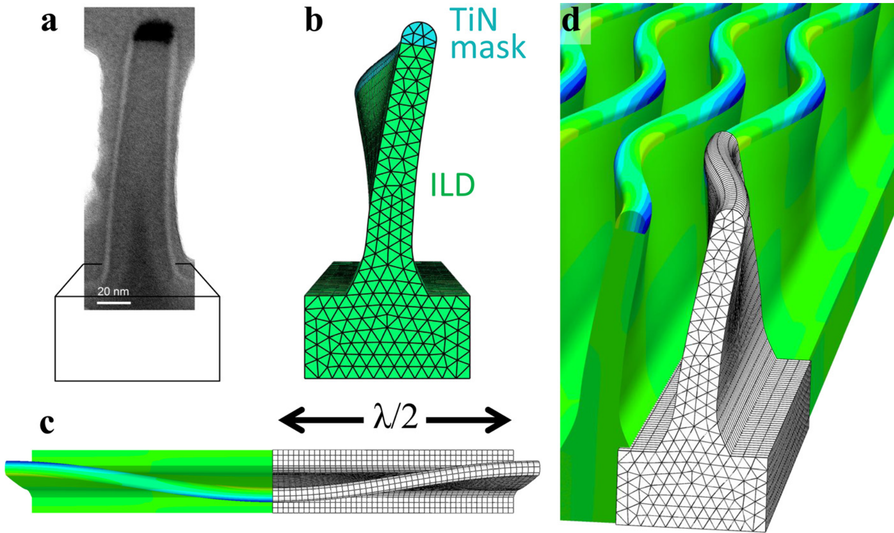

FIG. 6. Cross-sectional TEM and FEM images of deflection of sample S1. (a) Cross-section TEM of ILD wall and mask. (b) End of FEM of a simulated cross-section. (c) Top view of FEM showing $\lambda/2$ modeled segment and mirror image to create a single sinusoidal oscillation. (d) Oblique view of FEM showing assembly of $\lambda/2$ segments into buckled periodic structures. Coloring in (c) and (d) shows contours of elastic strain energy where the lowest energy indicated by blue occurs at the most deflected points.

B. Buckling FEM

Physical parameters and meaning for the longer-scale stochastic model were provided by a shorter-scale deterministic FEM analysis of buckling. Inputs for the FEM analysis from the longer scale included the characteristic wavenumber, q_0, and the measured mean-square deflection, $\overline{v^2}$. Additionally, the TEM-measured cross-sectional geometry (Sec. II B) was needed. The FEM simulation related the compressive TiN eigenstress, σ, to the buckling amplitude, A, and wavenumber, q, so that $\sigma = \sigma(A, q)$. The stress function is multiple valued for the stable state with zero buckling amplitude, $A = 0$. The FEM analysis was used to determine the ILD elastic modulus, E_{ILD}, the critical stress to buckle, σ_0, and the sensitivities of the buckling stress to variations in the deflection amplitude and buckling wavenumber, σ_{AA} and σ_{qq}, up to an unknown stress-scale set by the TiN Young's modulus, E_{TiN}. Published E_{TiN} values measured by contact stiffness[16] determined the FEM output values in an absolute sense. In this way, all parameters were determined using only measurements of the as-processed samples.

Examples of the finite element buckling model and cross-section geometries are shown in Fig. 6. The model was similar to those used in Refs. 13, 15, and 16, but with more precise ILD wall and mask geometries consistent with observed cross-sections. Ref. 15 notes that simple rectangular geometries can lead to erroneous predictions of buckling. Initial studies here found that simplified rectangular geometries and simplifying assumptions about mask-ILD mechanical coupling could introduce relative errors to extracted values as large 100% when compared with the outputs of more precise modelling. Initially, a stand-in value, $E_{\mathrm{TiN}} = 400\,\mathrm{GPa}$, was used to enable numerical model solution. For simplicity, typical Poisson's ratios were used, $\nu = 0.2$ for TiN and $\nu = 0.25$ for ILD materials. First, a linear buckling analysis was performed, and then a nonlinear finite buckling analysis.

The linear buckling FEM was used to solve for the critical buckling stress ratio, $\sigma_0/E_{\mathrm{TiN}}$, the ILD modulus ratio, $E_{\mathrm{ILD}}/E_{\mathrm{TiN}}$, and the stress sensitivity to wavenumber ratio, $\sigma_{qq}/E_{\mathrm{TiN}}$. The linear model had two parameters that could be varied, the ILD modulus, $E_{\mathrm{ILD}}/E_{\mathrm{TiN}}$, and the model length, $\lambda/2 = \pi/q$. Varying $\lambda/2$ while holding the ILD modulus constant allowed calculation of a buckling spectrum that related the compressive stress at the onset of buckling to the buckling wavenumber, q: $S(q) = \lim_{A\to 0^+} \sigma(A, q)$ (e.g., Fig. 7(a)). For each ILD modulus ratio, a buckling spectrum has a different minimum $S_{\min}$ at $q_{\min}$. The correct ratio was found by choosing $E_{\mathrm{ILD}}/E_{\mathrm{TiN}}$ such that $q_{\min} \to q_0$ (more details in Appendix D[45]). Next, the critical buckling stress ratio, $\sigma_0/E_{\mathrm{TiN}}$, was found as $S_{\min}/E_{\mathrm{TiN}}$.

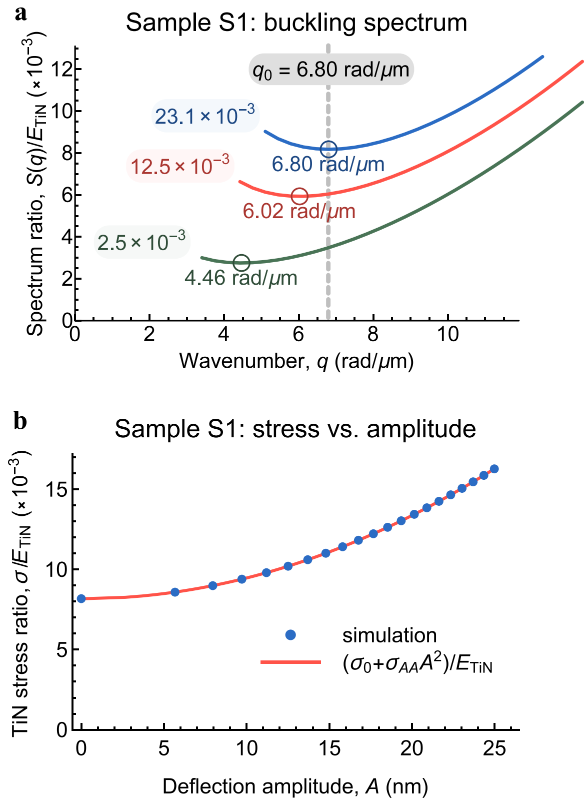

FIG. 7. FEM results for sample S1. (a) Simulated dimensionless buckling spectra relating stress ratio, S/E_{TiN}, to wavenumber, q. Boxed values indicate the corresponding modulus ratio, $E_{\mathrm{ILD}}/E_{\mathrm{TiN}}$, that gave rise to each spectrum. Spectrum minima are indicated by circles. The blue minimum coincides with characteristic wavenumber for sample S1 (gray dashed line). (b) Stress ratio vs. amplitude from finite deformation buckling simulation of sample S1 (blue symbols). Red line shows least-squares fit to obtain σ_{AA}/E_{TiN}.

Reuse of AIP Publishing content is subject to the terms at: https://publishing.aip.org/authors/rights-and-permissions. Download to IP: 129.6.180.62 On: Thu, 17 Mar 2016 12:30:09

Following the linear analysis, a nonlinear analysis was performed to find the stress-amplitude sensitivity ratio, $\sigma_{AA}/E_{\mathrm{TiN}}$. The model length was set to the characteristic value, $\lambda/2 = \pi/q_0$, and $E_{\mathrm{ILD}}/E_{\mathrm{TiN}}$ was set to the previously determined value. The stress-ratio *vs.* deflection amplitude has a parabolic shape (e.g., Fig. 7(b)). The parabolic shape verified the hypothesis of weak nonlinearity that underpins Eq. (1). Weak nonlinearity was further supported by the sinusoidal shape of the modeled buckling deflection (Fig. 6(c)). Fitting the stress-ratio vs. amplitude, the second stress-sensitivity ratio, $\sigma_{AA}/E_{\mathrm{TiN}}$, was found. Using published E_{TiN} measurements[16] (Table I), the resulting shorter-scale buckling behavior could then be summarized as

$$\sigma = \sigma_0 + \frac{1}{2}\sigma_{qq}(q - q_0)^2 + \sigma_{AA}A^2. \tag{3}$$

In the absence of random behavior, Eq. (3) would appear to contain the whole picture. In fact, it would be overcomplete, as variations in wavenumber q would not occur in homogeneous deterministic systems, and a simplified equation would result, $\sigma \to \sigma_0 + \sigma_{AA}A^2$.

In a prior study of microscale out-of-plane buckling, it was noted that large amplitudes affected the buckling wavelength where the amplitude-to-wavelength ratio ranged from 0.03 to 0.15.[21] In contrast, the nanoscale ILD wall deflections have amplitude to wavelength ratios that are less than 0.03, and the distinguishing feature is not wavelength sensitivity to amplitude, but rather irregularity (pseudo-periodicity) of the deflections arising from underlying stochastic fluctuations.

On inspection, it might appear that the deterministic formula, Eq. (3), could be applied to stochastic systems with judicious choices for A and q. A representative value for A might be chosen, such as the root-mean-square deflection amplitude, $A = (2\overline{v^2})^{1/2}$, similar to the procedure in Ref. 16. Therein, it was noted that stochastic effects probably explained departures from the model predictions. In the absence of a developed stochastic non-linear model, it was not possible to verify this hypothesis. Additionally, a wavenumber, q, that is continued into the complex plane might be chosen to take into account finite phase correlations so that $q \to q_0 + il^{-1}$. The resulting pseudo-stochastic stress relation would be $\sigma = \sigma_0 + 2\sigma_{AA}\overline{v^2} - \frac{1}{2}\sigma_{qq}l^{-2}$. Phenomenologically, this equation has a lot to offer. In the absence of stochastic effects, indicated by long range correlation, $l \to \infty$, larger deflections would indicate larger stress. Large stochastic effects, indicated by small correlation effects, would similarly allow buckling at stresses smaller than predicted from deterministic models alone, even sub-critical buckling, i.e., buckling at less than the critical stress, σ_0. Unfortunately, this approach has a number of shortcomings. First, simulations (Sec. III C) indicate that the pseudo-stochastic formula is quantitatively inaccurate. Second, simulations also indicate that higher-order statistics, $\overline{v^4}$, play an important role. Finally, without further simulation, it is impossible to validate the model through detailed comparisons with observed deflections. The pseudo-stochastic formula is not an alternative for performing longer-scale stochastic simulations.

C. Physical stochastic model

The final stage of the multiscale analysis was to implement the physical stochastic model. First, the physical significance and numerical values of the coefficients in Eq. (1) were determined. Then, stochastic forcing was added to the deflection model. Next, unknowns were found from statistical measures of the deflection pseudo-periodicity. Finally, the solved unknowns were used to simulate deflection profiles and validate the reduced parameter description of ILD trench-wall deflection.

The mathematical stochastic model is expressed by Eq. (1). With an appropriate choice for the coefficients and forcing term, $F(x)$, this model can be used to extend the findings of the deterministic shorter-scale model to the longer-scale domain. This extension was performed by considering the case of a force-free buckling deflection of wavenumber q and ensuring that the predictions of the longer-scale model were consistent with the shorter-scale findings. A perfectly coherent deflection in the absence of force with wavenumber q and constant amplitude A was considered, $v(x) = \mathrm{Re}(Ae^{iqx})$, so that $A(x) = Ae^{i(q-q_0)x}$. Inserting $A(x)$ and $F(x) = 0$ into Eq. (1) and then factoring out $A(x)$ results in Eq. (3), provided that σ_{AA} and σ_{qq} have the same value in both equations and that the characteristic square-amplitude in Eq. (1) is $A_0^2 = (\sigma - \sigma_0)/\sigma_{AA}$. (It is equally valid to choose a common proportionality constant for σ_{AA}, σ_{qq}, and A_0^2, but for the present purpose, it was most convenient to choose a proportionality constant of one.) Note that A_0^2 is negative for the subcritical buckling case as it is the *characteristic* square-amplitude, not the *mean* square-amplitude.

The next step was to determine the appropriate form of the stochastic forcing. In trying to choose the simplest form possible, qualitative comparison of simulation results with measured deflections indicated that a sum of two noise terms was needed: complex-valued additive white noise, $\eta_{\mathrm{a}}(x)$, and real-valued multiplicative white noise, $\eta_{\mathrm{m}}(x)$, so that the stochastic governing equation was

$$\left[-(\sigma - \sigma_0) + \sigma_{AA}|A(x)|^2 - \frac{1}{2}\sigma_{qq}\partial_x^2\right]A(x) = \eta_{\mathrm{m}}(x)A(x) + \eta_{\mathrm{a}}(x). \tag{4}$$

Using only additive white noise, $F(x) = \eta_{\mathrm{a}}(x)$, effectively reproduced the phase decorrelation but produced only negligible amplitude fluctuations. Using only multiplicative white noise, $F(x) = \eta_{\mathrm{m}}(x)A(x)$, resulted in substantial amplitude fluctuations but negligible phase decorrelation. Combining additive and multiplicative white noise effectively reproduced both phase decorrelation and amplitude fluctuations (Appendix C.4). While the specific physical causes of the noise terms are beyond the scope of this work and are not experimentally accessible, it is not difficult to see how such noise terms might arise. For example, fluctuations in stress level along the length of trench walls would give rise to real-valued multiplicative noise, while asymmetric stress fluctuations transverse to the trench walls would result in local bending moments that could be represented as additive complex noise. Additionally, it is expected that there would be

Reuse of AIP Publishing content is subject to the terms at: https://publishing.aip.org/authors/rights-and-permissions. Download to IP: 129.6.180.62 On: Thu, 17 Mar 2016 12:30:09

fluctuations in geometry and material properties along with their associated contributions to noise. Fig. 4 shows an example realization of a solution to Eq. (4). Numerical method details are given in Appendix C.3.[45]

As spatial variations in stress, geometry, and material properties were not directly measured, the physical stochastic model (Eq. (4)) initially had three unknown parameters, the sought after TiN mask stress, σ, and the amplitudes of the two noise terms. These three values were found by matching the statistical characterization of the solutions to Eq. (4) with the statistical measures from the two earlier stages: the mean square-deflection, $\overline{v^2}$, the phase correlation length, l, and the fourth moment of deflection, $\overline{v^4}$.

Using dimensional analysis and numerical simulations, it was possible to express the effects of the stochastic behavior on the quantity of most interest, the TiN hard mask stress. The TiN stress can be written as the naive stress-amplitude relation discussed in Sec. III C with a stochastic correction function, $f(r_{pd}, r_{af})$

$$\sigma = \sigma_0 + 2\sigma_{AA}\overline{\nu^2} f(r_{pd}, r_{af}), \quad (5)$$

where $r_{pd} = \frac{1}{4}\sigma_{qq} l^{-2}/\sigma_{AA}\overline{\nu^2}$ is the dimensionless measure of phase decorrelation and $r_{af} = \frac{2}{3}\overline{\nu^4}/(\overline{\nu^2})^2$ is the dimensionless measure of amplitude fluctuation (Appendix C.4 (Ref. 45)). Contours of $f(r_{pd}, r_{af})$ are shown in Fig. 8. In the absence of random fluctuations, the correction factor reverts to the deterministic case, $f(0, 1) = 1$. The noise amplitudes were found similarly (Appendix C.4 (Ref. 45)).

Applying this method in turn to each of the investigated samples, the dimensionless measures r_{pd} and r_{af} were calculated from the statistical measures and stress sensitivities. The correction factors were found numerically from the calculated values (Appendix C.4;[45] Fig. 8). The TiN mask stresses were calculated using Eq. (5). Finally, the fractional adjustment due to the stochastic analysis was calculated by comparing the final stress value with the value that would have been obtained by assuming no stochastic correction ($f(r_{pd}, r_{af}) \to 1$). See Table II for a summary and Table C1 (Ref. 45) for a complete set of parameters. Sample S2 demonstrates the important case of subcritical buckling: The stochastic correction factor for S2 is $f(r_{pd}, r_{af}) = -0.974$, so that the model-inferred TiN mask stress is 1.527 GPa, a value less than the critical buckling stress of 1.632 GPa. This subcritical buckling indicates that point-to-point variations in stress, properties, or geometry drove the ILD walls to buckle, not an excess of average stress.

Once the hard mask stresses and stochastic forcing amplitudes were determined, buckling deflection profiles were simulated for comparison with the measured deflections. Individual ILD trench-wall buckling profiles were used for qualitative comparison. Autocorrelations were obtained from large ensembles of simulated deflections (4000 simulations for each case) to give converged statistics. Examples of simulated deflection images are shown in Fig. 9. A more detailed comparison of individual deflections alongside example measured deflections is shown in Fig. 10.[45]

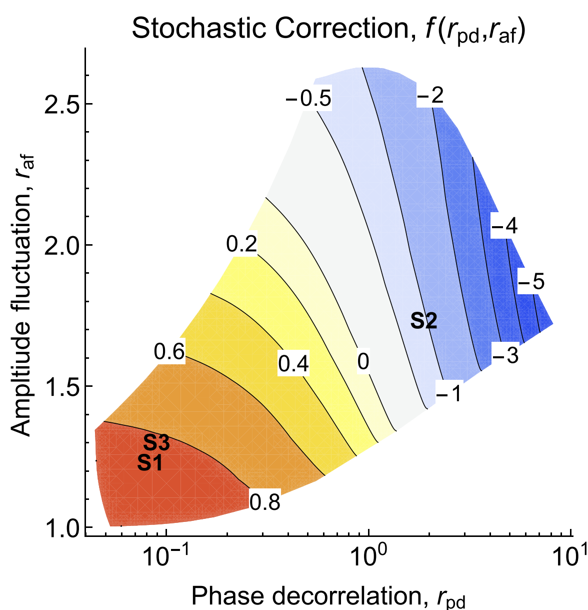

FIG. 8. Stochastic correction function calculated from dimensionless simulations. The stress correction for each sample (S1, S2, and S3) can be read from the contour plot using measured statistics of the phase decorrelation (r_{pd}) and amplitude fluctuation (r_{af}).

IV. DISCUSSION

The multiscale analysis and modeling depend on the notion that the entire ensemble of buckled ILD trench walls in each sample can be characterized by four meaningful statistical measures of the longer-scale random buckling

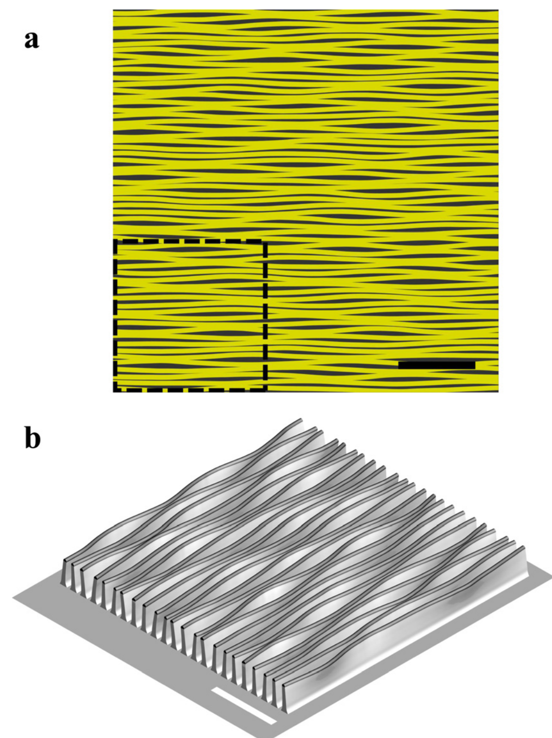

FIG. 9. Simulated ILD buckled wall images similar to sample S1. (a) Plan-view image similar to an AFM image (scale-bar is 1 μm). Dashed box shows reconstructed region in (b). (b) Three-dimensional image similar to an SEM image from simulated deflections and finite element calculations (scale-bar is 500 nm; Appendix C.5).

Reuse of AIP Publishing content is subject to the terms at: https://publishing.aip.org/authors/rights-and-permissions. Download to IP: 129.6.180.62 On: Thu, 17 Mar 2016 12:30:09

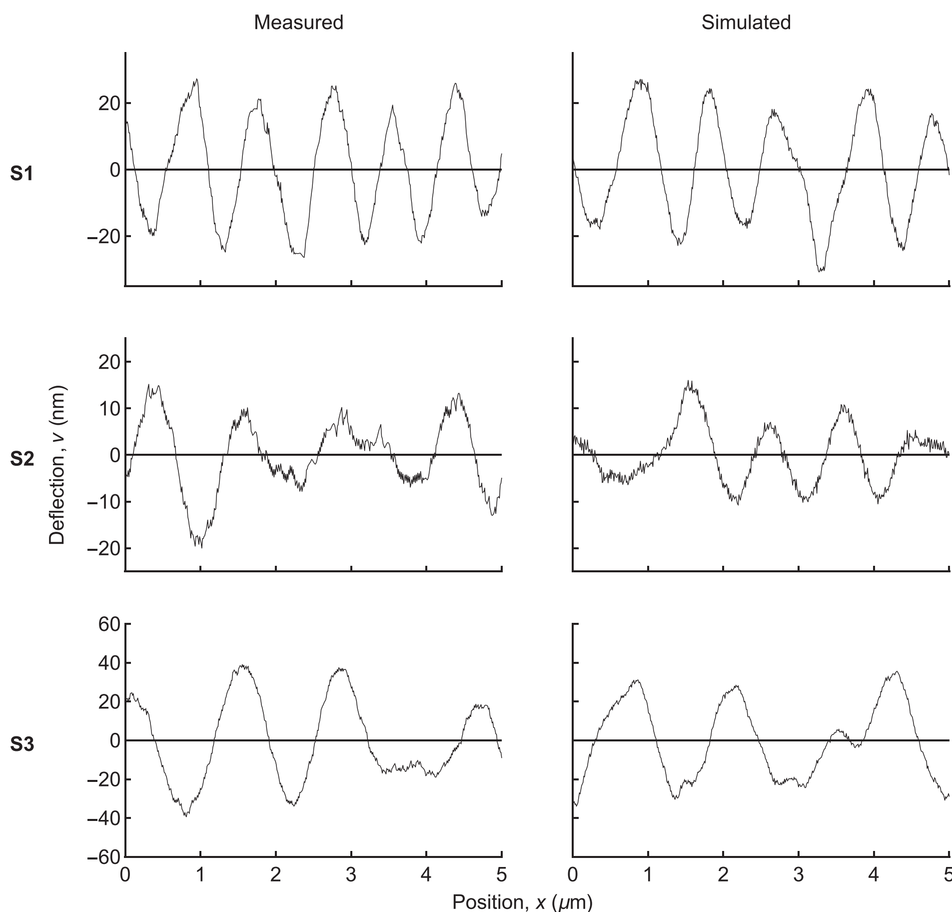

FIG. 10. Measured and simulated deflections. Measurements are deflections from samples S1, S2, and S3. Simulated deflections use physical parameters extracted from nonlinear multiscale stochastic method. (Multimedia view) [URL: http://dx.doi.org/10.1063/1.4943615.1][45]

(q_0, l, $\overline{v^2}$, $\overline{v^4}$) and a clear understanding of the shorter-scale buckling mechanics (characterized by σ_0, σ_{AA}, and σ_{qq}). The success of this approach was tested in a number of ways: First, qualitative visual aspects of simulated buckling were compared with images and measured deflections. Second, the statistics of simulated ensembles were compared with those obtained from measurements. Finally, the values of physical quantities extracted from the multiscale model were compared with those from measurements where available. Each of these aspects is now examined, followed by considerations of the application of the current approach in ILD engineering and to other systems.

A. Qualitative and statistical deflection comparisons

The simulated trench-wall deflections show a strong qualitative resemblance to their measured counterparts. Figure 9(a) shows an image of an ensemble of simulated buckled walls (using sample S1 parameters) presented in a format comparable to the AFM images of Figs. 1(c) and 1(d). Figure 9(b) shows an image of an enlarged section of Fig. 9(a) presented in a format comparable to the scanning electron microscope (SEM) image of Fig. 1(b). Although rendering in both simulated images has been deliberately selected to enable favorable comparison with the experimental images, it is clear that the simulation has captured the look of the within- and between-wall buckling variability. A more detailed assessment is shown in side-by-side comparisons for all three samples of measured and simulated deflections in Fig. 10.[45] The simulated deflections do an excellent job of capturing the differences and commonalities of buckling in each sample, and there are no glaringly omitted characteristics despite the fact that the simulations represent random realizations corresponding to only four measured parameters.

The study reported here corroborates the hypothesis of subcritical buckling;[16] however, no stochastic effect on wavelength was found, nor is it clear why there should be such an effect. Stochastic effects would appear first at the wavelength of maximum compliance unless the driving noise was severely colored. Rather, it would appear that wavelength is difficult to predict for the as-processed materials. As the present study includes detailed finite element modeling and measurement of the as-processed samples, it is concluded that the etching process affects material properties that ultimately change the expected buckling wavelengths (see Section IV B).

In even greater detail, the statistical deflection comparison of Fig. 5 shows that the longer-scale model does an excellent job of capturing the long-range behavior. The approximate envelope function, Eq. (2), is an excellent fit to the long-range decay of the measured autocorrelations. The simulated autocorrelations showed even more aspects of agreement than the initial four statistical measures. Autocorrelations were calculated from ensembles of 4000 realizations corresponding to each sample and the average response shown as the black solid lines in Fig. 5; the agreement in both amplitude and phase with the experimental

Reuse of AIP Publishing content is subject to the terms at: https://publishing.aip.org/authors/rights-and-permissions. Download to IP: 129.6.180.62 On: Thu, 17 Mar 2016 12:30:09

autocorrelation, shown as the grey bands, is clear. Thus, the three parameter model, depending on $\overline{v^2}$, l, and q_0, for the autocorrelation is fully justified, gives a complete description of both the experimental and simulated autocorrelations, and serves as a valid link between measurable stochastic behavior and physical understanding and materials parameter determination.

B. Physical quantities

The etched ILD trench walls with hard-mask had undergone some various harsh processing procedures making it difficult to compare the *in-situ* determination of physical quantities here with other *ex-situ* measurements. However, these comparisons can still be used to gauge the reasonableness of inferred quantities and perhaps might provide insight into how processing might affect materials properties and state.

For samples S1 to S3, Eq. (5) gave compressive TiN mask stresses that were greater than those indicated by wafer curvature measurements prior to etching (Table III). Given the thinness of the TiN masks and the documented effect that ion bombardment has on TiN film stress,[52] the observed stress increase resulting from the plasma etch steps is not surprising. Furthermore, the fractional effect of stochastic analysis was to lower the stress estimated in every case. If stochastic effects had been neglected (i.e., assuming $f = 1$), the inferred stresses would have been erroneous and even greater by 5%–15%. Different elastic moduli were found for TiN on different ILD materials (Table I): about 230 GPa for TiN on a-SiOC:H (sample S1) and about 155 GPa for TiN on a-C:H (samples S2 and S3). The large difference in the elastic moduli of TiN of these samples suggests a specific reactivity of TiN to various substrates. It has been also shown that mechanical properties of TiN are very sensitive to stress and stoichiometry.[53,54]

In comparing the ILD Young's moduli with mechanical measurements of similar ILD blanket films, some difference was expected between the measurements due to variation in deposited ILD films, measurement error, and possible damage of the ILD trench walls from the plasma etch, yet the measured moduli turn out to be quite close (Table III). For sample S1, E_{ILD} from the multiscale stochastic method compared well with Brillouin light scattering measurements of blanket a-SiOC:H.[42] For samples S2 and S3, E_{ILD} was a little greater than similar measurements on similar blanket ILD films (a-C:H).[42]

C. Application in ILD engineering and extensibility to other phenomena

The success of the stochastic multiscale analysis in characterizing the observed buckling suggests that the analysis and its associated models have a role in further ILD trench engineering, and that the design of ILD trenches might need to be approached differently. The prior deterministic approach has been to keep mean design criteria such as stress and aspect ratio at subcritical levels.[13] This criterion has zero-tolerance for buckling. However, as demonstrated by the behavior and stress of sample S2, such a criterion is untenable. There will always be some level of underlying randomness; therefore, there will always be some amount of subcritical buckling. For structures of larger dimensions, subcritical instability may be so small as to be immeasurable, but at the nanoscale this is not the case. Sample S2 would pass all mean design criteria and still fail as a usable structure. Going forward, design criteria should probably be expressed as a maximum tolerance for buckling, either as an allowable mean-square deflection or perhaps a maximum density of deflections greater than some threshold value. Predictive design must estimate the degree of effective randomness resulting from process and material variability. Such an estimate would require further study of simulations and *post mortem* failure analyses such as those presented here.

In this work, a stochastic multiscale method was applied to an instance in which it was not possible to measure or fully understand the origins of stochastic behavior at the length scales smaller than those experimentally measured. However, the strength of the stochastic fluctuations was measured indirectly through their effect on larger-scale observations. As mentioned previously, the central limit theorem states that incorporation of random analyses will become a more pressing need with the maturation of nanoscale science and technology and the work here is an example of such an analysis. While results such as those presented in Fig. 8 may be applied directly to one-dimensional problems with the G-L form, Eq. (4), for other problems[54] the presented method can serve as heuristic guide. Other opportunities to apply stochastic methods in a similar manner have already been mentioned.[25–31] In cases where stochastic

TABLE III. Measured and extracted physical properties of buckled wall materials.

	Sample S1	Sample S2	Sample S3
TiN stress from wafer curvature, σ (GPa)[a]	1.4	1.0	1.0
TiN stress, inferred, σ (GPa)[b]	2.68	1.520	1.978
Fractional stochastic stress correction[b] (%)	−5.8	−15.3	−9.0
ILD modulus from Brillouin light scattering, E_{ILD} (GPa)	5.7[c]	2.5[d]	2.5[d]
ILD modulus, inferred, E_{ILD} (GPa)[b]	4.85	4.54	4.71

[a]Values from wafer curvature prior to etching.[16]
[b]Values from present stochastic multiscale analysis (TABLE II).
[c]Value from blanket a-SiOC:H film similar to ILD of sample S1.[39]
[d]Value from blanket a-C:H film similar to ILD of samples S2 and S3.[39]

Reuse of AIP Publishing content is subject to the terms at: https://publishing.aip.org/authors/rights-and-permissions. Download to IP: 129.6.180.62 On: Thu, 17 Mar 2016 12:30:09

effects have been homogenized away,[35–39] incorporating sensitivity factors and using the available *a priori* shorter-scale fluctuations may provide greater insight and more precise and robust prediction of material behavior.

V. CONCLUSION

We have presented a nonlinear multiscale stochastic method that was shown to effectively simulate nano-scale buckled ILD trench walls with a stressed TiN hard mask and to extract mechanical information from mechanical stiffness measurements and geometric and morphological information at both long and short length-scales. The multi-scale approach allowed us to investigate how randomness influenced measured structural behavior and inferences about properties without direct knowledge of the underlying sources of random behavior. Dimensionless measurable quantities were defined that characterized observed longer-scale random fluctuations using sensitivity parameters from shorter-scale modeling. A deterministic model relating stress to observed behavior was corrected to incorporate the stochastic nature of the observed buckling. The model was validated both qualitatively and quantitatively through simulated statistics and deflections and agreement with experimental observations.

This approach demonstrates a tremendous advantage over linear approaches, over single-scale stochastic approaches, and over multi-scale models that attempt to homogenize shorter-scale randomness. Linear approaches cannot simulate the buckled state, so they are difficult to fully validate. Single-scale stochastic approaches require microscopic understanding of randomness that is impossible to obtain in most cases. Approaches that homogenize away stochastic fluctuation will frequently give results that are not comparable to observed behavior and that ignore the impact that stochastic fluctuations can have on quantitative inferences. The technique demonstrated here is applicable to the development of nanoscale ILD technology for microelectronic interconnects, and more broadly for increasing the accuracy of measurements and models that are confounded by randomness that is inevitable at the nanoscale.

ACKNOWLEDGMENTS

The authors thank S. King (Intel, Inc.) for provision of the cross-sectioned TEM samples, G. Stan (NIST) for provision of the raw AFM trench wall deflection data, and M. Vaudin (NIST) for provision of the SEM micrograph.

[1]F. Reif, *Fundamentals of Statistical and Thermal Physics* (McGraw-Hill Kogakusha, Tokyo, 1965).
[2]R. J. Barlow, *Statistics* (John Wiley & Sons, Chichester, 1989).
[3]H. G. Craighead, Science **290**, 1532 (2000).
[4]E. A. Carter, Science **321**, 800 (2008).
[5]S. J. L. Billinge and I. Levin, Science **316**, 561 (2007).
[6]M. D. Uchic, D. M. Dimiduk, J. N. Florando, and W. D. Nix, Science **305**, 986 (2004).
[7]D. Jang and J. R. Greer, Nat. Mater. **9**, 215 (2010).
[8]M. M. J. Treacy, T. W. Ebbesen, and J. M. Gibson, Nature **381**, 678 (1996).
[9]G. Stan, C. V. Ciobanu, P. M. Parthangal, and R. F. Cook, Nano Lett. **7**, 3691 (2007).
[10]J. H. Panchal, S. R. Kalidindi, and D. L. McDowell, Comput.-Aided Des. **45**, 4 (2013).
[11]D. Edelstein, J. Heidenreich, R. Goldblatt, W. Cote, C. Uzoh, N. Lustig, P. Roper, T. McDevitt, W. Motsiff, A. Simon, J. Dukovic, R. Wachnik, H. Rathore, R. Schulz, L. Su, S. Luce, and J. Slattery, in *Tech. Dig. Int. Electron Devices Meet. (IEDM 97)* (1997), pp. 773–776.
[12]K. Maex, M. R. Baklanov, D. Shamiryan, F. Lacopi, S. H. Brongersma, and Z. S. Yanovitskaya, J. Appl. Phys. **93**, 8793 (2003).
[13]M. Darnon, T. Chevolleau, O. Joubert, S. Maitrejean, J. C. Barbe, and J. Torres, Appl. Phys. Lett. **91**, 194103 (2007).
[14]M. van Veenhuizen, G. Allen, M. Harmes, T. Indukuri, C. Jezewski, B. Krist, H. Lang, A. Myers, R. Schenker, and K. J. Singh, in *IEEE Int. Interconnect Technol. Conf. (IITC)* (2012), pp. 1–3.
[15]J. Ducoté, N. Possémé, T. David, M. Darnon, T. Chevolleau, and M. Guillermet, Appl. Phys. Lett. **104**, 231603 (2014).
[16]G. Stan, C. V. Ciobanu, I. Levin, H. J. Yoo, A. Myers, K. Singh, C. Jezewski, B. Miner, and S. W. King, Nano Lett. **15**, 3845 (2015).
[17]R. C. Hibbeler, *Mechanics of Materials*, 7th ed. (Pearson Prenctice Hall, Upper Saddle River, 2008).
[18]P. J. Yoo, K. Y. Suh, S. Y. Park, and H. H. Lee, Adv. Mater. **14**, 1383 (2002).
[19]C. M. Stafford, C. Harrison, K. L. Beers, A. Karim, E. J. Amis, M. R. VanLandingham, H.-C. Kim, W. Volksen, R. D. Miller, and E. E. Simonyi, Nat. Mater. **3**, 545 (2004).
[20]D.-Y. Khang, H. Jiang, Y. Huang, and J. A. Rogers, Science **311**, 208 (2006).
[21]H. Jiang, D.-Y. Khang, J. Song, Y. Sun, Y. Huang, and J. A. Rogers, Proc. Natl. Acad. Sci. U. S. A. **104**, 15607 (2007).
[22]J. A. Rogers, T. Someya, and Y. Huang, Science **327**, 1603 (2010).
[23]P. Cendula, S. Kiravittaya, Y. F. Mei, C. Deneke, and O. G. Schmidt, Phys. Rev. B **79**, 085429 (2009).
[24]J. Dervaux and M. Ben Amar, J. Mech. Phys. Solids **59**, 538 (2011).
[25]N. Bowden, S. Brittain, A. G. Evans, J. W. Hutchinson, and G. M. Whitesides, Nature **393**, 146 (1998).
[26]X. Chen and J. W. Hutchinson, J. Appl. Mech. **71**, 597 (2004).
[27]R. Huang, J. Mech. Phys. Solids **53**, 63 (2005).
[28]V. R. Tirumala, C. M. Stafford, L. E. Ocola, J. F. Douglas, and L. Mahadevan, Nano Lett. **12**, 1516 (2012).
[29]Z. Y. Huang, W. Hong, and Z. Suo, J. Mech. Phys. Solids **53**, 2101 (2005).
[30]S. Cai, D. Breid, A. J. Crosby, Z. Suo, and J. W. Hutchinson, J. Mech. Phys. Solids **59**, 1094 (2011).
[31]M. Şimşek and H. H. Yurtcu, Compos. Struct. **97**, 378 (2013).
[32]Z.-F. Huang, K. R. Elder, and N. Provatas, Phys. Rev. E **82**, 021605 (2010).
[33]L. H. Friedman, J. Electron. Mater. **36**, 1546 (2007).
[34]V. R. Vedula, S. J. Glass, D. M. Saylor, G. S. Rohrer, W. C. Carter, S. A. Langer, and E. R. Fuller, J. Am. Ceram. Soc. **84**, 2947 (2001).
[35]W. K. Liu, L. Siad, R. Tian, S. Lee, D. Lee, X. Yin, W. Chen, S. Chan, G. B. Olson, L.-E. Lindgen, M. F. Horstemeyer, Y.-S. Chang, J.-B. Choi, and Y. J. Kim, Int. J. Numer. Methods Eng. **80**, 932 (2009).
[36]M. R. Maschmann, G. J. Ehlert, S. Tawfick, A. J. Hart, and J. W. Baur, Carbon **66**, 377 (2014).
[37]Y. Wei, J. Mech. Phys. Solids **70**, 227 (2014).
[38]M. Z. Jin and C. Q. Ru, Phys. Rev. E **88**, 012701 (2013).
[39]W. Chen, Z. Liu, H. M. Robinson, and J. Schroers, Acta Mater. **73**, 259 (2014).
[40]C. S. Nichols, R. F. Cook, D. R. Clarke, and D. A. Smith, Acta Metall. Mater. **39**, 1667 (1991).
[41]S. W. King, M. French, M. Jaehnig, M. Kuhn, and B. French, Appl. Phys. Lett. **99**, 202903 (2011).
[42]W. Zhou, S. Bailey, R. Sooryakumar, S. King, G. Xu, E. Mays, C. Ege, and J. Bielefeld, J. Appl. Phys. **110**, 043520 (2011).
[43]S. Bailey, E. Mays, D. J. Michalak, R. Chebiam, S. King, and R. Sooryakumar, J. Phys. D: Appl. Phys. **46**, 045308 (2013).
[44]Certain commercial equipment, instruments, or materials are identified in this document. Such identification does not imply recommendation or endorsement by the National Institute of Standards and Technology nor does it imply that the products identified are necessarily the best available for the purpose.
[45]See supplementary material at http://dx.doi.org/10.1063/1.4943615 for Appendices, Figs. A1 and C1, Table C1, and multimedia file.
[46]D. E. Newland, *An Introduction to Random Vibrations, Spectral & Wavelet Analysis*, 3rd ed. (Dover Publications, 2005).

Reuse of AIP Publishing content is subject to the terms at: https://publishing.aip.org/authors/rights-and-permissions. Download to IP: 129.6.180.62 On: Thu, 17 Mar 2016 12:30:09

[47]C. W. Gardiner, *Handbook of Stochastic Methods for Physics Chemistry and the Natural Sciences*, 3rd ed. (Springer, New York, 2004).
[48]M. C. Cross and P. C. Hohenberg, Rev. Mod. Phys. **65**, 851 (1993).
[49]A. C. Newell and J. A. Whitehead, J. Fluid Mech. **38**, 279 (1969).
[50]L. A. Segel, J. Fluid Mech. **38**, 203 (1969).
[51]I. S. Aranson and L. Kramer, Rev. Mod. Phys. **74**, 99 (2002).
[52]D. Mao, K. Tao, and J. Hopwood, J. Vac. Sci. Technol., A **20**, 379 (2002).
[53]F. Vaz, J. Ferreira, E. Ribeiro, L. Rebouta, S. Lanceros-Méndez, J. A. Mendes, E. Alves, P. Goudeau, J. P. Riviere, and F. Ribeiro, Surf. Coat. Technol. **191**, 317 (2005).
[54]A. A. Golovin, S. H. Davis, and P. W. Voorhees, Phys. Rev. E **68**, 056203 (2003).

Reuse of AIP Publishing content is subject to the terms at: https://publishing.aip.org/authors/rights-and-permissions. Download to IP: 129.6.180.62 On: Thu, 17 Mar 2016 12:30:09